A study of the impact of dislocations on the thermoelectric properties of quantum wells in the Si/SiGe materials system

Jeremy R. Watling[a] and Douglas J. Paul
School of Engineering, University of Glasgow, Glasgow G12 8LT, United Kingdom

(Received 3 August 2011; accepted 23 October 2011; published online 5 December 2011)

Thermoelectric materials generate electricity from thermal energy using the Seebeck effect to generate a voltage and an electronic current from a temperature difference across the semiconductor. High thermoelectric efficiency *ZT* requires a semiconductor with high electronic conductivity and low thermal conductivity. Here, we investigate the effect of scattering from threading dislocations of edge character on the thermoelectric performance of individual *n* and *p*-channel SiGe multiple quantum well structures. Our detailed physical simulations indicate that while the thermal and electrical conductivities decrease with increasing dislocation scattering/density, the Seebeck coefficient actually increases with increasing threading dislocation density above 10^6 cm^{-2} at room temperature, due to an increase in the entropy associated with each carrier. The collective result of these individual effects, is that the present Si-based quantum well designs can tolerate scattering by a threading dislocation density up to $\sim 10^8$ cm^{-2}, well within the capabilities of modern growth techniques, before significant reductions in *ZT* due to scattering from threading dislocations is observed. © *2011 American Institute of Physics*. [doi:10.1063/1.3665127]

I. INTRODUCTION

Thermoelectric devices and materials are able to generate electricity from thermal energy using the Seebeck effect. A temperature difference across the material results in a voltage and electron current being developed that is dependent on the Seebeck coefficient of the material and the size of the temperature gradient across the device. *n*- and *p*-type semiconductors have Seebeck coefficients with opposite polarities which are typically tens or hundreds of μV/K and so to produce an electric circuit, separate *n* and *p*-type thermoelectric components are connected in series to form a thermoelectric module, as illustrated schematically in Fig. 1. The individual modules can then be connected together electrically in series and thermally in parallel to produce useful voltages and currents. A complete thermoelectric generator might contain many tens or even hundreds or thousands of individual modules depending on the application.

Thermoelectric materials have been used since the 1960s and the corresponding Peltier effect is heavily used to produce coolers for telecommunication lasers and high power solid-state sources.[1] As sustainable energy becomes more important as the cost of fossil fuels increases, many new potential applications for thermoelectric generators are being studied including energy harvesting in cars, industrial plants but also for self-powered autonomous sensing systems. The thermodynamic efficiency of present commercial thermoelectric generators based on bulk materials such as Bi_2Te_3 and Sb_2Te_3 is small. Low dimensional systems have been suggested to provide higher performance that may allow thermoelectrics to become competitive with other technologies.[2]

Thermoelectric performance is commonly measured by employing the dimensionless figure of merit *ZT* where *T* is the absolute temperature. The thermoelectric figure of merit *Z* measured in units of T^{-1} is given by

$$Z = \frac{\sigma S^2}{(\kappa_{el} + \kappa_{ph})}, \tag{1}$$

where σ denotes the electrical conductivity and κ_{el} and κ_{ph} the electronic and phononic contributions to the thermal conductivity, respectively. *S* denotes the Seebeck coefficient (sometimes called the thermoelectric power). The calculation of these individual factors is discussed in further detail later in the text.[3]

At present, however, most thermoelectric devices are based on bulk material properties, limiting the *ZT*, in part due to the Wiedemann-Franz Law, which linearly relates the electrical and thermal conductivities for heavily doped, metallic semiconductors.[4] Significantly higher *ZTs*, however, can be obtained for low dimensional structures using quantum wells, wires or dots. In order to produce practical devices, however, it is necessary for a large number of $\gg$100 of these quantum well layers to be considered. Ge has a 4.2% larger lattice constant than Si, and therefore, thermoelectric designs using $Si/Si_{1-x}Ge_x$ heterostructures ($0 \leq x \geq 1$) are limited by the critical thicknesses for each heterolayer as well as the complete stack of strained layers.[5] Thus, strained balanced quantum well structures must be utilised, as all practical layer thicknesses for a complete thermoelectric generator are significantly greater than the critical thickness of the heterolayers.[6] Although, some/many aspects of the thermal and electrical transport maybe considered to be independent of the exact fabrication process implemented, two important scattering mechanisms which can depend on the exact nature of the quality of the epitaxial growth are interface roughness and dislocation scattering, these two mechanisms are related to some degree.[7,8] The effect of interface

[a]Electronic mail: Jeremy.Watling@glasgow.ac.uk.

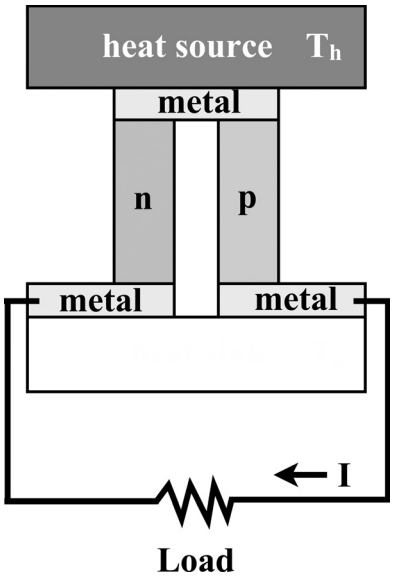

FIG. 1. An individual thermoelectric module requires separate *n* and *p*-type thermoelectric components to produce an electrical circuit between two thermal reservoirs. The hot reservoir has a temperature of T_h and the cold reservoir has a temperature of T_c to provide a temperature gradient across the semiconductor legs of the module.

roughness scattering on thermal conductivity has been studied previously,[9,10] although little has been done in the context of thermoelectrics directly where it is important to consider both electrical and thermal transport. However, for strain-balanced multiple quantum well superlattices, the formation of a number of threading edge dislocations is inevitable and dislocations are likely to play a dominant role, in determining the feasibility of such structures.[5]

Only a few results have been reported of the experimental performance of $Si/Si_{1-x}Ge_x$ heterostructures thermoelectric designs[11–13] while there have been many reports of reduced thermal conductivity in Si/SiGe superlattice structures (e.g., Ref. 14). *p*-type designs require either a Ge channel quantum well or a $Si_{1-x}Ge_x$ quantum well in a $Si_{1-y}Ge_y$ matrix where $x > y$.[6] For *n*-type designs, the options are far wider and both Si quantum wells and Ge quantum wells are possible by the band structure of the system.[5] Strain symmetrised designs will require a buffer with an intermediate Ge composition compared to the barrier and quantum well compositions. This buffer should ideally be as thin as possible to minimise thermal conductivity of the buffer but unfortunately, thin buffers normally have significantly higher dislocation densities compared to thick graded buffers .[5] For example, the growth of a Ge heterolayer well above the critical thickness will result in threading edge dislocations densities over 10^{11} cm^{-2} to accommodate the lattice mismatch if no special techniques are used to reduce this value.[5] Thick graded buffers can provide threading dislocation densities below 10^6 cm^{-2} but thick buffers are expensive to grow and provide a small thermal resistance that is detrimental to thermoelectric devices. The use of low temperature growth heterolayers to help nucleate dislocations as well as thermal annealing can reduce this density to around 10^7 cm^{-2} (Ref. 15) and limited area growth provides values as low as 2.3×10^6 cm^{-2} (Ref. 16) have been demonstrated. Significantly, lower threading dislocation densities are achievable for materials of smaller lattice mismatch, for example, relaxed $Si_{0.8}Ge_{0.2}$ on Si where values as low as 5000 cm^{-2} have been reported.[17]

The aim of this work is to investigate the dependence of thermoelectric $Si/Si_{1-x}Ge_x$ heterostructure designs consisting of separate *n* and *p*-type $Si/Si_{1-x}Ge_x$ quantum well structures to different levels of threading dislocation densities. Dislocation densities from values below reported densities up to the maximum values reported in the literature will be studied to determine the potential increase in performance if lower dislocation density buffers could be developed. Although other crystal defects such as stacking faults and crystal defects may well be present in such structures, these are not considered here, as they are likely to be localised in nature. Thus, they will not play such an important role in determining the net thermoelectric properties of the structure as compared to the global nature of the threading dislocations. The designs presented here are aimed at room temperature operation (~300 K) and this temperature is assumed in all the results presented. The work deliberately does not include interface roughness scattering at present to allow the direct effect of dislocations without other significant competing mechanisms to be analysed and therefore allow maximum values of threading dislocations to be determined for high thermoelectrics performance. Nevertheless, interface roughness scattering still remains an important issue in relation to thermoelectrics and will be the subject of a future paper.

II. P-CHANNEL LATERAL QUANTUM WELL DESIGN

We employ here a strained quantum well structure to maximise the electrical conductivity through the reduced effective mass due to strain as well as reduced ionized impurity scattering through doping in the barriers, while still maintaining a high carrier concentrations within the quantum wells. In order to provide a large electrical conductivity, it is necessary to have a repeated structure of quantum wells and barriers, this can be achieved through strain symmetrisation of the quantum wells and barriers,[6] the thicknesses for which may be calculated as follows:

$$\frac{h_A}{h_B} = \frac{G_B}{G_A}\left[\frac{a_B - a_A}{a_A(a_{sub}/a_A)} - 1\right], \tag{2}$$

where $h_A(h_B)$ represents the heterolayer thickness of the tensile (compressive) strained layer. $G_A(G_B)$ is the shear modulus of the tensile (compressive) strained layer; $a_B(a_A)$ represents the relaxed lattice constant of the tensile (compressive) strained layers and a_{sub} the relaxed lattice constant of the virtual substrate. The design discussed here is a repeated series of 17.5 nm $Si_{0.3}Ge_{0.7}$ barriers containing a thin boron (7.5 nm) doped layer (10^{18} cm^{-3}) in the middle of the barrier, with an undoped 9 nm Ge quantum well as grown on a relaxed $Si_{0.2}Ge_{0.8}$ relaxed buffer. The advantages of this structure are that the electrical conductivity will be dominated by the Ge quantum well, which are known to exhibit high electrical conductivities,[18,19] while the thermal conductivity will be dominated by the relatively thick barriers,

which will possess a thermal conductivity significantly less the Ge quantum well.[20]

III. N-CHANNEL LATERAL QUANTUM WELL DESIGN

The design presented here for the *n*-channel design is similar in nature to that presented for the *p*-channel design above. It consists of a repeated series of 12.5 nm $Si_{0.5}Ge_{0.5}$ barriers containing a thin arsenic (6.5 nm) doped layer (10^{18} cm^{-3}) in the middle of the barrier, with an undoped 8 nm Si quantum well as grown on a relaxed $Si_{0.7}Ge_{0.3}$ buffer layer. This structure is chosen so as to provide the best confinement for the lowest lying energy bands in this case the Δ_2 bands, as the Si quantum well is under a net tensile strain, within the constraints of strain-balancing. This type of structure should provide good electrical conductivity within the Si quantum well structures.[21,22]

IV. MODELLING OF THE ELECTRICAL CONDUCTIVITY

To obtain an estimate of the thermoelectric effect associated with carrier and phonon transport perpendicular to the growth direction, parallel to the heterointerfaces, we require both the electrical and thermal conductivity in this direction, as the electric field parallel to the quantum well interface is likely to be small (within the regime for which a low-field linear mobility maybe defined) we may calculate the electrical conductivity within each individual quantum subband *i* by employing the Kubo-Greenwood formalism.[23–25] We first define the mobility within each subband at a given energy *E*

$$\mu_i(E) = \frac{2e}{3n_i}\rho_i(E)E\tau(E)m_{ci}(E)^{-1}\left(\frac{\partial f_0}{\partial E_F}\right), \tag{3}$$

from which we may define the electrical conductivity for each subband as[26]

$$\sigma_i = e\int_0^\infty \rho_i(E)\mu_i(E)f_0(E)(1-f_0(E))dE. \tag{4}$$

The total electrical conductivity may be calculated as follows:

$$\sigma = \frac{\sum_{i=1}^{N} n_i\sigma_i}{\sum_{i=1}^{N} n_i}. \tag{5}$$

In the above expressions, *e* is the magnitude of the electron charge, *n* is the carrier density and $\tau(E)$ is the total momentum relaxation for the carriers with energy *E* (this will be a sum over all the individual scattering mechanisms, we considered here all the major scattering mechanisms:[27] inelastic acoustic, optical phonon, alloy scattering, along with scattering from edge dislocations,[28] which we will consider in detail later.) $m_c(E)$ is the conductivity effective mass parallel to the heterointerfaces, distinct from the confinement mass in the growth direction $\rho_i(E)$ is the two-dimensional density of states associated with the particular sub-band, E_F is the Fermi-energy and $f_0(E)$ is the Fermi Dirac distribution function.

In order to maintain the essential features of the $Si_{1-x}Ge_x$ band structure, while still being able to maintain sufficient flexibility to be able to provide a reasonable understanding of the important factors controlling performance and efficiency within such device structures, we employ an ellipsoidal (with distinct effective masses perpendicular and parallel to the heterointerfaces) non-parabolic mass band-model for each of the individual hole-bands and electron bands. Such an approach has been shown to be sufficient for capturing the essential physics of carrier transport in such layers, while still maintaining computational efficiency.[29] For the hole-bands, the appropriate directional effective masses extracted from a multi-band (**k.p**) model,[30] using the approach outlined in Ref. 31 are used, while the electron masses that take into the account the appropriate variations with strain are taken from Ref. 32. These masses are then employed within a self-consistent solution of the coupled Poisson and Schrödinger equations as described in Ref. 27, employing an extrapolated convergence factor method as described in Ref. 33 to calculate the wavefunction envelopes of the carriers within the $Si_{0.3}Ge_{0.7}$/Ge quantum well superlattice. It should be noted that both the anisotropy in the effective masses and the physical nature of the superlattices discussed here will mean that both the thermal and electrical conductivity will be anisotropic, exhibiting different behavior perpendicular and parallel (the component calculated here) to the heterointerfaces. From these, the relaxation rates/times for all the relevant mechanisms can be determined.

V. MODELLING OF THE THERMAL CONDUCTIVITY

The total thermal conductivity of the devices being considered will have contributions both from the acoustic phonons and also from the transport of the carriers (electrons or holes). This contribution will be important and dominate within the quantum wells due to the high carrier concentrations present, whilst the transport of acoustic phonons will dominate within the barrier regions.

The thermal conductivity due to the transport of the electronic carriers κ_{iel} (holes in this instance) for a given subband *i* is determined by the following expression:[34]

$$\kappa_{iel} = \frac{\sigma}{e^2T}\left[\frac{\langle\tau\rangle\langle E^2\tau\rangle - \langle E\tau\rangle^2}{\langle\tau\rangle^3}\right], \tag{6}$$

where the angular brackets $\langle\,\rangle$ denote an appropriate energetic averaging of the quantities concerned, the symbols are as described previously.

In order to calculate the phonon contribution to the thermal conductivity, κ_{ph} we employ Callaway's expression for the thermal conductivity[35–37]

$$\kappa_{ph} = \frac{k_B}{2\pi^2}\left(\frac{k_B}{\hbar}\right)^3 T^3\int_0^{\theta_D/T}\frac{\tau_C(x)x^4e^x}{\nu(x)(e^x-1)^2}dx, \tag{7}$$

where k_B is the Boltzmann constant, $\hbar$ is Planck's constant divide by 2π, θ_D is the Debye temperature, *x* is dimensionless

variable $x = \hbar\omega/k_BT$, τ_C is the combined phonon relaxation time and v denotes the velocity. In order to determine a reliable estimate of the thermal conductivity particularly when θ_D is comparable to T, as is the case here $\theta_D \sim 640$ K for Si and $\sim$374 K for Ge,[38] it is necessary to consider the entire acoustic phonon dispersion. In this work we consider the charge carriers as confined two-dimensional quantum entities. Phonons (acoustic and optical) are considered within a three-dimensional framework. Kubakaddi and co-workers[39–41] have previously demonstrated the applicability of such an approach to be of value in the situation and length-scales considered in the present designs. The acoustic phonon dispersion is modelled using the analytical description of Fischer.[42] We consider here the following dominant processes for phonon scattering: Umklapp scattering,[43,44] impurity scattering due to the acceptors, arising from the presence of atoms with different atomic masses,[44] alloy scattering and dislocation scattering. The scattering of phonons in many of the relaxation time mechanisms is dominated by the Grüneisen parameter γ within the limits of the available experimental data,[38,45] we treat this as an adjustable parameter to obtain a close fit to the thermal conductivity of both bulk Si and Ge at 300 K.

VI. CALCULATION OF THE THERMOELECTRIC POWER

Finally, in order to determine Z (and ZT), we need to determine the Seebeck coefficient, S. This is calculated using for each individual sub-band i the following expression:[34]

$$S_i = \frac{1}{(eT)}\left[\frac{\langle E\tau\rangle}{\langle\tau\rangle} - E_F\right]. \tag{8}$$

The total effective Seebeck coefficient is determined by employing the procedure as for the electrical conductivity as given by Eq. (5). The sign of the Seebeck coefficient can also be used to determine the sign of the charge carriers within the sample: for holes the Seebeck coefficient is positive, while for electrons the Seebeck coefficient is negative.

VII. DISLOCATION SCATTERING

Edge dislocations set up a corresponding strain field around them with the atoms displaced from their equilibrium positions in a perfect crystal. The approach followed here is based on the model described in Ref. 46, however, we extend the model to account for a general quantum well bias, rather than the flat quantum well considered previously. The shift in the valence band edge for a given strain is given by

$$\Delta E = a_V Tr(\varepsilon), \tag{9}$$

a_v denotes the hydrostatic valence band deformation potential, $Tr(\varepsilon)$ is the trace of the strain matrix. A similar expression can be derived for the conduction band. The strain distribution radiating outward from an edge dislocation is given by[47]

$$\Delta = -\frac{b_C}{2\pi}\frac{1-2\nu}{1-\nu}\frac{\sin(\theta)}{r}. \tag{10}$$

Here, b_c is the magnitude of the Burgers vector for the edge dislocation, and ν is the Poisson ratio for the crystal. Combining this with the equation above, we can obtain the resulting perturbing potential, the Fourier transform of which, forms the main part of the scattering matrix element for determining the corresponding momentum relaxation scattering rate as given by

$$\frac{1}{\tau_{dis}} = \frac{N_{disl}(1+2\alpha E)b_c^2}{4\pi\hbar^3}\left(\frac{1-2\nu}{1-\nu}\right)^2\int_0^{2\pi}\frac{H_{i,mn}(q)}{q^2}(1-\cos\theta)d\theta, \tag{11}$$

where q represents the change in the momentum k parallel to the hetero-interface of the quantum well, N_{disl} is the dislocation density and $H_{i,mn}(q)$ is given by

$$H_{i,mn}(q) = \iint \psi_{i,m}(z_1)\psi_{i,n}(z_1)\psi_{i,m}(z_2)\psi_{i,n}(z_2) \exp(-q|z_1 - z_2|)dz_1dz_2. \tag{12}$$

In this equation, $\Psi_{i,n}(z)$ is the n-th subband eigenfunction in the i-th valley. Inter-valley scattering due to dislocation scattering has been neglected since the scattering rate for such transitions is very small due to the large momentum transfer involved. In the above equation, summing the square of the matrix element over all scatterers in the dilute scattering limit, leads to an averaging of the angular averaged over the angle ϕ between q and the Burgers vector b_c for all different dislocations, such an averaging yields $\langle\sin^2(\phi)\rangle = 1/2$.[28] The affect of dislocation scattering in terms of phonons (heat flow) is also accounted for using a similar approach.[48]

VIII. IMPACT OF DISLOCATION SCATTERING ON THE SEEBECK COEFFICIENT AND ELECTRICAL AND THERMAL CONDUCTIVITIES.

In this section, we look at the impact of dislocation scattering on the individual components of the thermoelectric figure of merit: Seebeck coefficient and the electrical and thermal conductivities. First, we look at the impact of dislocation scattering on the Seebeck coefficient as shown in Fig. 2. Strictly speaking we show here only the magnitude of the Seebeck coefficient, as mentioned previously the Seebeck coefficient is negative for electrons. We observe similar characteristics for both the n and p-type designs with the Seebeck coefficient increasing with dislocation density (an increase of $\sim$30% and 50% for the n and p-type, respectively) until saturation occurs at $\sim 10^{10}$ cm^{-2}. This increase may be understood from Eq. (8). The value of the relaxation time $\langle\tau\rangle$ decreases with increasing dislocation density as is to be expected, leading to a corresponding decrease in the electrical conductivity as observed in Fig. 3. However, if we expand the term in the numerator $\langle E\tau\rangle$ as: $\langle E\tau\rangle = \langle E\rangle\langle\tau\rangle + C_{E\tau}$, where $C_{E\tau}$ is the correlation between energy and the momentum relaxation time, it is clearly this term that determines the increase in the Seebeck coefficient. In the case of dislocation scattering this is positive, which is characteristic of electrical interactions, where as can be seen from the Eq. (11) the momentum relaxation time will

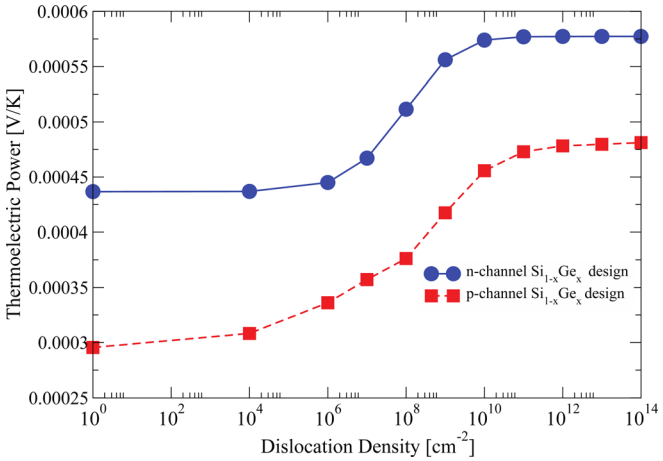

FIG. 2. (Color online) The Seebeck coefficient S (VT^{-1}) as a function of the dislocation density from 0 to 10^{14} cm^{-2} for the n-channel design (blue solid-line with circles) and p-channel design (red dashed-line with circles).

increase with increasing energy. The end result is that the Seebeck coefficient increases with increasing dislocation scattering until dislocation scattering becomes the dominant scattering mechanism. A useful physical interpretation here for the Seebeck coefficient or thermoelectric power is that it provides a measure for the entropy per charge carrier within the material.[3,49] The observed increase in Fig. 2 can be understood as the dislocation scattering increasing the entropy or randomness associated with the charge carrier flow within the system leading in turn to an increase in the Seebeck coefficient.

Next, we look at the effect of dislocation scattering on the thermal conductivity as shown in Figs. 4(a) and 4(b), respectively. Fig. 4(a) shows the phonon contribution to the thermal conductivity κ(W/Km) for the p-channel $Si_{1-x}Ge_x$ design, while Fig. 4(b) illustrates the same for the n-channel $Si_{1-x}Ge_x$ design. As mentioned previously the electrical conductivity (Fig. 3) decreases with increasing dislocation density, we also observe a similar effect in the thermal conductivity as shown in Figs. 4(a) and 4(b). The thermal

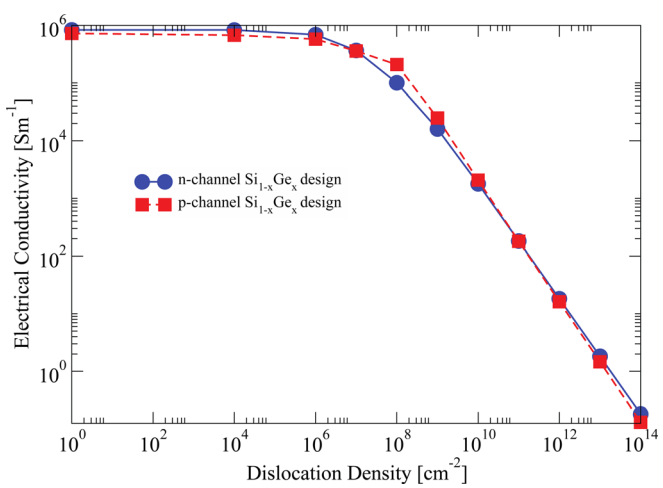

FIG. 3. (Color online) The electrical conductivity (S/cm) as a function of the dislocation density from 0 to 10^{14} cm^{-2} for the p-channel design discussed in the text.

conductivity here in the absence of dislocation scattering is dominated by phonon-Umklapp scattering, along with alloy scattering and scattering from the doping-impurities within the barriers, as is usual in semiconductors, except in the limit of very high carrier concentrations. Although, we include the electronic contribution to the thermal conductivity, we find that it only plays a minor role (~1.2% and ~3.5% for the n and p-type designs, respectively) and is therefore not required for understanding the results. Additionally, for strained materials the velocity of sound is changed to allow for the changes in the lattice volume between relaxed and strained (ΔVol). Therefore, the velocity of sound for the strained material (U_{Strained}) is given by

$$U_{\text{Strained}} = U_{\text{Relaxed}}\sqrt{\left(1 \pm \frac{\Delta Vol}{Vol_{\text{Relaxed}}}\right)}. \tag{13}$$

The $\pm$ takes into account whether the net change in the volume is positive or negative, according to the type of strain (compression or tensile), and the Young's Moduli of the material.

In both the n and p-type designs, the thermal conductivity is higher within the quantum wells as in both cases these are undoped, in order to maximize electrical conductivity. The quantum wells are both of a pure elemental type (Si for n-type and Ge for p-type), thus, the effects of both alloy scattering and impurity scattering are both absent. However, it is the total weighted-averaged thermal conductivity that is important in terms of determining the effectiveness of the thermoelectric figure of merit. Thus, the lower thermal conductivity of the thick barriers plays an important role in determining the averaged thermal conductivity. While the electrical conductivity is dominated by the characteristics of the quantum well, the thick $Si_{1-x}Ge_x$ barriers dominate the thermal conductivity. The quantum well superlattice enables us thus to improve the thermo-electric coefficient over bulk materials, by allowing us to improve the electrical conductivity, with a reduction in the thermal conductivity to obtain a higher σ/κ ratio than would be achievable for bulk materials.

The thermal conductivity of the Si quantum well in the n-type design though is considerably higher than for the Ge quantum well in the p-type design, thus leading to an approximately ~2.5–3 times higher thermal conductivity in the n-type design as compared to the p-type design. Despite the increased Seebeck coefficient, this results in the n-type design having a slightly poorer ZT than the p-type design. We notice though that while the thermal conductivity of the Ge quantum well is relatively high as is common in many good electrical conductors, it is the thermal conductivity of the $Si_{0.3}Ge_{0.7}$ barriers that dominates the average thermal conductivity, due to the larger width of the barriers as compared to the quantum wells.

We observe that both the electrical and thermal conductivities remain relatively stable at low dislocations density and then begin to drop sharply as the threading dislocation density begins to become the dominant scattering mechanism for both electrical ($>10^8$ cm^{-2} dislocation density) and

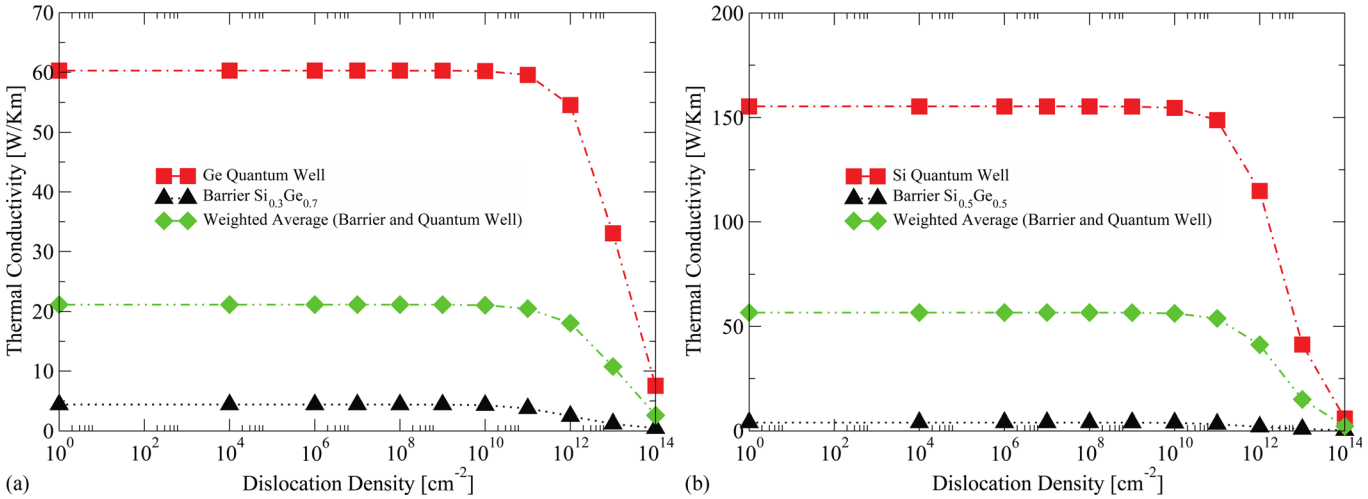

FIG. 4. (Color online) (a) The phonon contribution to the thermal conductivity κ (W/Km) as a function of the dislocation density from 0 to 10^{14} cm^{-2} for the *p*-channel $Si_{1-x}Ge_x$ design discussed in the text. The individual contributions are denoted as follows: The thermal conductivity for the strained Ge quantum wells: (red squares). The thermal conductivity for the $Si_{0.3}Ge_{0.7}$ barriers: (black triangles). The weighted average of the thermal conductivity for the quantum wells and barriers: (green diamonds). (b) The phonon contribution to the thermal conductivity κ(W/Km) as a function of the dislocation density from 0 to 10^{14} cm^{-2} for the *n*-channel $Si_{1-x}Ge_x$ design discussed in the text. The individual contributions are denoted as follows: The thermal conductivity for the strained Si quantum wells: (red squares). The thermal conductivity for $Si_{0.5}Ge_{0.5}$ barriers: (black triangles). The weighted average of the thermal conductivity for the quantum wells and the barriers: (green diamonds)

thermal ($>10^{10}$ cm^{-2} dislocation density) conductivities, with the electrical conductivity exhibiting the greatest decrease. This results in a sharp decrease in the ratio of the electrical to thermal conductivities, which cannot be compensated for by the associated increase in the Seebeck coefficient (thermoelectric power), indeed due to the dominance of the dislocation density the Seebeck coefficient has begun to saturate within this region.

IX. IMPACT OF DISLOCATION SCATTERING ON THE THERMO-ELECTRIC DESIGN OF THE N AND P-TYPE QUANTUM WELLS

The dependence of *ZT* for our designs is evaluated for threading dislocation densities from 1×10^4 cm^{-2} to 1×10^{14} cm^{-2}. This is sufficient to cover the published range

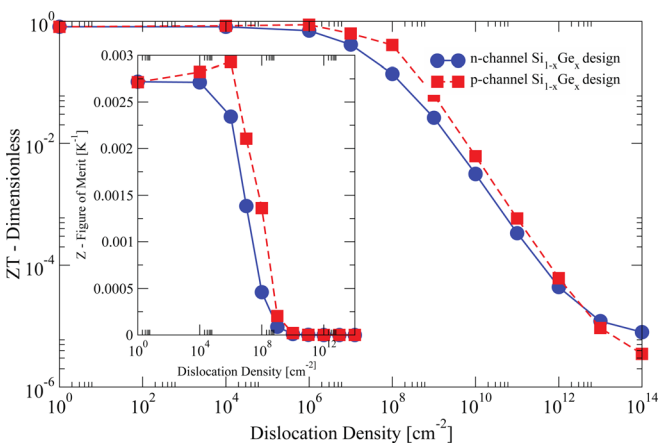

FIG. 5. (Color online) The dimensionless thermoelectric figure of merit *ZT* (T = 300 K assumed) as a function of the dislocation density from 0 to 10^{14} cm^{-2} for the *n*-channel design (blue solid-line with circles) and the *p*-channel design (red dashed-line with circles) as discussed in the text. The thermoelectric figure of merit Z (T^{-1}) as a function of the same dislocation density is shown in the inset.

of dislocation densities obtained in the growth of strained Ge heterolayers on Si. These dislocation densities vary from 1×10^6 cm^{-2} to 1×10^{10} cm^{-2} (Refs. 50 and 51) the variation being dependent on the substrate thickness and growth conditions. The effect of the dislocation scattering on the thermoelectric figure of the dimensionless figure of merit *ZT* ($T = 300$ K assumed) for the individual designs is shown in Fig. 5, for both the *p*-channel and *n*-channel designs. We can clearly see that for both electrons and holes that the effect of dislocation scattering has little effect on the dimensionless figure of merit, below a dislocation density of $\sim 10^8$ cm^{-2}. Above this density, dislocation scattering becomes increasingly important and the thermoelectric figure of merit drops rapidly. Below a dislocation density of $\sim 10^8$ cm^{-2}, the figure or merit for the holes actually increases by a small amount as can be seen most clearly from the insert in Fig. 5, which shows the figure of merit *Z*. The reason for this is that although dislocation scattering has a negative impact on both electrical and thermal transport, the critical factor is the ratio of the electrical to the thermal conductivity as compared to the Seebeck coefficient. As discussed in the previous section the mechanism for this small increase is due to an enhancement in the Seebeck coefficient from dislocation scattering, Fig. 2, as the Seebeck coefficient is associated with the entropy per charge carrier.

X. CONCLUSIONS

We have investigated the impact of the dislocation density for both components of a quantum well $Si/Si_{1-x}Ge_x$ thermoelectric module consisting of *n*-channel and *p*-channel $Si/Si_{1-x}Ge_x$ quantum well structures. We have shown that the thermoelectric figure of merit for both the *n* and *p*-channel components remains acceptable for many applications up to a dislocation density of $\sim 10^8$ cm^{-2} and then decreases rapidly.

This may be understood by the fact that after a dislocation density of $\sim 10^8$ cm^{-2} dislocation scattering starts to become the dominate scattering mechanism for charge carriers (electrons and holes). Thus, the electrical conductivity begins to decrease sharply with increasing dislocation density at the same time as the Seebeck coefficient increase starts to saturate. After a dislocation density of $\sim 10^8$ cm^{-2} the decrease in the electrical conductivity and eventual saturation of the Seebeck coefficient begin to dominate and the thermoelectric figure of merit is correspondingly degraded. In conclusion, our designs exhibit an acceptable tolerance to dislocation scattering, a major issue limiting the practical fabrication of large superlattices, for densities up to and including 10^8 cm^{-2}. This information is extremely useful as it shows that such a proposed superlattice may be fabricated with relative ease, as similar strained SiGe superlattices have been previously fabricated with dislocation densities lower than the limiting value presented here. This work also sets an upper limit for the dislocation density in thin SiGe strain relaxation buffer layers for thermoelectric devices that any new technology aimed at thermoelectrics must be able to meet if high performance thermoelectric generators are to be produced.

ACKNOWLEDGMENTS

The work was funded by the EC ICT Future Emerging Technologies Proactive Initiative "Towards Zero Power ICT" under project GREEN Silicon (Project No. 257750).

[1]D. M. Rowe, *Thermoelectrics Handbook: Macro to Nano* (CRC, Taylor and Francis Group, New York, 2005).
[2]L. D. Hicks and M. S. Dresselhaus, Phys. Rev. B **47**, 12727 (1993).
[3]A. F. Ioffe, *Semiconductor Thermoelements and Thermoelectric Cooling* (Infosearch, London, 1957).
[4]N. W. Ashcroft and N. D. Mermin, *Solid State Physics* (McGraw-Hill Book Company, W. B. Saunders Company, Philadelphia, 1976).
[5]D. J. Paul, Semicond. Sci. Technol. **19**, R75 (2004).
[6]D. J. Paul, Laser Photonics Rev. **5**, 610 (2010).
[7]S. B. Samavedam and E. A. Fitzgerald, J. Appl. Phys. **81**, 3108 (1997).
[8]D. Choi, Y. Ge, J. S. Harris, J. Cagnon, and S. Stemmer, J. Cryst. Growth **310**, 4273 (2008).
[9]P. Martin, Z. Aksamija, E. Pop, and U. Ravaioli, Phys. Rev. Lett. **102**, 125503 (2009).
[10]P. Martin, Z. Aksamija, E. Pop, and U. Ravaioli, Nano. Lett. **10**, 1120 (2010).
[11]X. Sun, S. B. Cronin, J. Liu, K. L. Wang, T. Koga, M. S. Dresselhaus, and G. Chen, in *Proceedings on the 18th International Conference on Thermoelectrics* (IEEE, Piscataway, New Jersey, 1999), p. 652.
[12]G. Zeng, A. Shakouri, C. L. Bounty, G. Robinson, E. Croke, P. Abraham, X. Fan, H. Reese, and J. E. Bowers, IEEE Electron. Lett. **35**, 2146 (1999).
[13]Y. Zhang, J. Christofferson, A. Shakouri, G. Zeng, J. E. Bowers, and E. T. Croke, IEEE Trans. Compon. Packag. Technol. **29**, 395 (2006).
[14]S. T. Huxtable, A. R. Abramson, C. Tien, A. Majumdar, C. LaBounty, X. Fan, G. Zeng, J. E. Bowers, A. Shakouri, and E. T. Croke, Appl. Phys. Lett. **80**, 1737 (2002).
[15]D. D. Cannon, J. Liu, Y. Ishikawa, K. Wada, D. T Danielson, S. Jongthammanurak, J. Michel, and L. C. Kimerling, Appl. Phys. Lett. **84**, 906 (2004).
[16]H. C. Luan, D. R Lim, K. K Lee, K.M Chen, J. G. Sandland, K. Wada, and L. C. Kimerling, Appl. Phys. Lett. **75**, 2909 (1999).
[17]A. De Rossi, M. Carras, and D. J Paul, IEEE J. Quantum Electron. **42**, 1233 (2006).
[18]M. Myronov, D. R. Leadley, and Y Shiraki, Appl. Phys. Lett. **94**, 092108 (2009).
[19]K. Sawano, K. Toyama, R. Masutomi, T. Okamoto, N. Usami, K. Arimoto, K. Nakagawa, and Y. Shiraki, Appl. Phys. Lett. **95**, 122109 (2009).
[20]J. P. Dimsukes, L. Ekstrom, E. F. Steigmeier, I. Kudman, and D. S. Beers, J. Appl. Phys. **35**, 2899 (1964).
[21]A. C. Churchill, D. J. Robbins, D. J. Wallis, N. Griffin, D. J. Paul, A. J. Pidduck, W. Y. Leong, and G. M. Williams, J. Vac. Sci. Technol.B, **16**, 1634 (1998).
[22]Th. Vogelsang and K. R. Hofmann, Appl. Phys. Lett. **63**, 186 (1999).
[23]R. Kubo, J. Phys. Soc. Jpn. **12**, 570 (1957).
[24]D. A. Greenwood, Proc. Phys. Soc. London **71**, 585 (1958).
[25]G. Ghibaudo, Phys. Status Solidi **153**, K155 (1989).
[26]H. Fritzche, Solid State Commun. **9**, 1813 (1971).
[27]J. R. Watling, A. B. Walker, J. J. Harris, and J. M. Roberts, Semicond. Sci. Technol. **13**, 43 (1998).
[28]D. Jena and U. K. Mishra, Appl. Phys. Lett. **80**, 64 (2002).
[29]M. V. Fischetti and S. E. Laux, Phys. Rev. B **48**, 2244 (1993).
[30]D. J. Paul, Phys. Rev. B **77**, 155323 (2008).
[31]F. M. Bufler, P. Graf, and B. Meinerzhagen, VLSI Des. **8**, 41 (1998).
[32]M. M. Rieger and P. Vogl, Phys. Rev. B **48**, 14276 (1993).
[33]F. Stern, J. Comput. Phys. **6**, 56 (1970).
[34]B. R. Nag, *Electron Transport in Compound Semiconductors* (Springer-Verlag, New York, 1980).
[35]J. Callaway, Phys. Rev. **113**, 1046 (1959).
[36]M. G. Holland, Phys. Rev. **132**, 2461 (1963).
[37]J. E. Parrott and A. D. Stuckes, *Thermal Conductivity of Solids* (Methuen, New York, 1975).
[38]*Landolt-Börnstein Group III Condensed Matter: Semiconductors A1: Group IV Elements, II-VI and III-V Compounds, Part β: Electronic, Transport, Optical and Other Properties*, Complete Edition of Vols. III/17a, 22a, and 41A1β on CD-ROM, edited by U. Rössler, (2002).
[39]S. S. Kubakaddbi, B. G. Mulimani, and V. M. Jali, Phys. Status Solidi B **137**, 683 (1986).
[40]V. M. Jali, S Kubakaddi, and B. G. Mulimani, Phys. Status Solidi B **137**, 267 (1986).
[41]S. S. Kubakaddbi, B. G. Mulimani, and N. S. Sankeshwar, Phys. Status Solidi B **142**, 135 (1987).
[42]B. Fischer and K. R. Hofmann, Appl. Phys. Lett. **74**, 2185 (1999).
[43]P. G. Klemens, *in Solid State Physics Vol. 7*, edited by F. Seitz and D. Turnbull (Academic, New York, 1958).
[44]Y. J. Han and P. G. Klemens, Phys. Rev. B **48**, 6033 (1993).
[45]J. Philip and M. A. Breazeale, J. Appl. Phys. **54**, 752 (1983).
[46]D. Jena and U. K. Mishra, Appl. Phys. Lett. **80**, 64 (2002).
[47]A. H. Cotterell, *Dislocations and Plastic Flow in Crystals* (Oxford University Press, Oxford United Kingdom, 1953).
[48]P. G. Klemens, Proc. Phys. Soc. A **68**, 1113 (1955).
[49]M. W. Zemansky and R. H. Dittman, *Heat and Thermodynamics* (McGraw-Hill, New-York, 1996).
[50]H. C. Luan, D. R. Lim, K. K. Lee, K. M. Chen, J. G. Sandland, K. Wada, and L.C Kimerling, Appl. Phys. Lett. **75**, 2909 (1999).
[51]S.R Jan, C. Y. Chen, C. H. Lee, S. T. Chan, K. L. Peng, C. W. Liu, Y. Yamamoto, and B. Tillack, Appl. Phys. Lett. **98**, 141105 (2011).